PEM Fuel Cell Characterization by Means of the Physical Model for Impedance Spectra

Tatyana Reshetenko[a],[*] and Andrei Kulikovsky[b],[c],[*],[z]

[a]*Hawaii Natural Energy Institute, University of Hawaii, Honolulu, Hawaii 96822, USA*
[b]*Forschungszentrum Juelich GmbH, Institute of Energy and Climate Research, IEK-3: Electrochemical Process Engineering, D-52425 Jülich, Germany*
[c]*Moscow State University, Research Computing Center, 119991 Moscow, Russia*

A recent analytical solution of the physical model for the PEM fuel cell impedance [A. A. Kulikovsky, *J. Electrochem. Soc.*, **162**, F217 (2015)] is used for least–squares fitting of experimental impedance spectra. Ten spectra are collected in one experimental run of a cell with ten segments operated at a current density of 100 mA cm^{-2} under high stoichiometry of the oxygen flow. The model impedance is fitted to the spectra and the resulting physical parameters of the cathode side are discussed. Of particular interest is a low value of the oxygen diffusion coefficient in the cathode catalyst layer ($\simeq 0.45 \cdot 10^{-4}$ cm^2 s^{-1}), a parameter, which has not been measured in situ so far. This low value, as well as a high value of the cathode catalyst layer (CCL) proton conductivity $\sigma_p \simeq 0.054 \ \Omega^{-1}$ cm^{-1} is attributed to a large amount of liquid water in the CCL.

In a large variety of modern electrochemical and physical methods for polymer electrolyte membrane fuel cells (PEMFCs) characterisation only a few allow for in situ measurements. The most widely used techniques of that type are measuring of the cell polarization curve and impedance spectra. Of largest interest is the cathode side of the cell, which consumes most part of the open–circuit potential. While polarization curve shows the sum of the potential losses V_{loss} on the cathode side and in the membrane, impedance measurements can separate the contributions of various processes to V_{loss}. This ability of electrochemical impedance spectroscopy (EIS) makes it an indispensable tool for the cell characterization.

A widely used approach to impedance spectra processing is the equivalent circuit method. An electric circuit consisting of R, C and L elements together with more complex electrochemical elements is constructed and fitted to the measured spectra.[1, 2] The electrochemical elements represent classic solutions for impedance of a planar electrode immersed in a liquid electrolyte.[3] However, there is no guarantee that the selected equivalent circuit is unique. Further, the relation of fitted electric parameters to the basic physical parameters of the cell components (transport coefficients, Tafel slope etc.) is beyond the scope of this approach. Last but not least, it can be shown that the classic electrochemical solutions do not, in general, describe the impedance of the porous PEMFC electrode.[4]

To resolve these problems, over the past two decades a lot of efforts has been made to develop numerical physical models for the cell impedance.[5–15] However, these models either ignore oxygen and proton transport in the cathode catalyst layer (CCL) or, if this transport is accounted for, they include numerical solution of boundary value problems for the distribution of static variables and their perturbations through the CCL depth. This makes the respective fitting codes slow, which retards their use in massive processing of experimental spectra.

Based on the classic works of deLevie[16] and Lasia,[17, 18] Eikerling and Kornyshev[19] developed an analytical physical model for the PEMFC cathode impedance. However, the solutions[19] are obtained assuming negligible transport of either protons, or oxygen in the cathode catalyst layer (CCL), and[19] ignores the potential loss due to the oxygen transport in the gas–diffusion layer (GDL).

Under real operating conditions, PEM fuel cell exhibits inhomogeneities in local performances due to fuel/oxidant consumption along the flow channel, accumulation of water, degradation and buildup of impurities. A segmented cell system is powerful tool for understanding locally resolved details of various processes, e.g., current distribution,[20–25] gas and water management effects,[26–30] defect detection and localization,[31–33] recirculation,[34] start–up and starvation effects,[35–38] CO poisoning effects[39–43] and other diagnostic techniques.[44–46] Further elaboration of the segmented cell approach resulted in development of locally resolved electrochemical impedance spectroscopy, which aids optimization of an electrode design, performance improvement and provides in situ characterization of inhomogeneity of membrane electrode assembly's properties.[27, 2847–50]

Recently, an exact analytical solution for the impedance of the cathode side of a PEM fuel cell has been derived, which includes proton and oxygen transport in the CCL, and the oxygen transport in the GDL.[4] In this work, we use this analytical expression for fast least–squares fitting of experimental impedance spectra acquired with the segmented PEM fuel cell operated under high stoichiometry of the oxygen flow. Fitting directly gives the basic transport and kinetic parameters of the cell. In this work, the segmented cell is used to obtain good statistics by measuring spectra for ten segments simultaneously. This approach is a first step toward local PEMFC characterization using the physics–based EIS under real operating conditions.

Experimental

The experiments have been performed on a single cell test station using Hawaii Natural Energy Institute's (HNEI) segmented cell system.[45] The segmented cell approach used in his study follows the ideas developed in.[20,21, 48, 51, 52] HNEI's system is partially based on the LANL design[20, 48] using closed loop Hall sensors and an improved data acquisition system. These enhancements allow the system to perform simultaneous measurements of spatial EIS, linear sweep voltammetry (LSV) and cyclic voltammetry (CV).[45]

The segmented cell system consists of the cell hardware, the custom designed current transducer system, the data acquisition device and a single cell test station (Figure 1). A closed loop Hall sensor (Honeywell CSNN 191) is employed for current sensing. The system allows the data collection from 10 current channels in a high (standard) current mode and from 16 channels in a low current mode. The standard current mode enables the measurement of segment current densities up to 2 A cm^{-2}. The low current mode yields measurement of current up to 50 mA cm^{-2}, which is typical for electrochemical diagnostics (CV and LSV). Voltage and current signal data collection was performed with a National Instrument PXI data acquisition instrument operating on HNEI–developed LabView programs.

This diagnostic tool is operated as a single fuel cell using a GRandalytics test station. Standardized single fuel cell testing protocols were used for recording spatially resolved data. All experiments were carried out under galvanostatic control of the total cell current.

[*]Electrochemical Society Active Member.
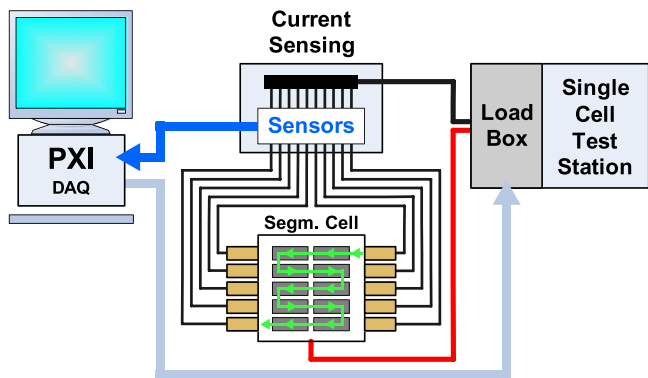[z]E-mail: A.Kulikovsky@fz-juelich.de

Figure 1. Segmented cell measurement setup. Reproduced from Ref. 45.

The segmented cell hardware consists of ten flow field segments forming a continuous path along ten parallel serpentine channels. Each segment is equipped with its own current collector and GDL and it has an area of 7.6 cm^2. The segmented cell hardware is applicable to either the anode or the cathode. The same channel designs are used for both the segmented cathode and the standard anode flow fields (the reactant streams were arranged in a co–flow configuration). More details on the hardware can be found in.[45]

The segmented cell was operated with commercially available 100 cm^2 membrane/electrode assembly (MEA) from Gore. The Pt/C loading of the anode and cathode electrodes was 0.4 mg$_{Pt}$ cm^{-2}. Sigracet 25 BC was used as the anode and cathode gas diffusion layers (GDLs). The cathode used a segmented GDL and gasket configuration, whereas a uniform GDL was applied at the anode. The total active area of MEA was 76 cm^2. The gasket material was made of Teflon, with thicknesses of 125 μm for the anode and cathode.

The segmented cell was assembled, conditioned and tested by making the polarization curve measurements. The anode/cathode conditions were pure hydrogen/oxygen at 2/9.5 stoichiometry, 100/50% relative humidity and 48.3/48.3 kP gauge backpressure. The cell temperature was 80°C. The frequency range for the EIS measurements was 0.1 Hz to 10 kHz and the amplitude of the sinusoidal current perturbation was 2 A, which resulted in the amplitude of the cell voltage response of 10 mV or lower. The impedance spectra were collected at the cell current density of 100 mA cm^{-2}.

Model

Model description.— Detailed description of performance and impedance models used in this work is given in Ref. 4; here we briefly outline the models. The transient CCL model includes the proton current conservation equation (1), the Ohm's law for the proton current density (2), and the oxygen mass balance equation (3):

$$C_{dl} \frac{\partial \eta}{\partial t} + \frac{\partial j}{\partial x} = -i_* \left(\frac{c}{c_h} \right) \exp \left(\frac{\eta}{b} \right) \quad [1]$$

$$j = -\sigma_p \frac{\partial \eta}{\partial x} \quad [2]$$

$$\frac{\partial c}{\partial t} - D \frac{\partial^2 c}{\partial x^2} = -\frac{i_*}{4F} \left(\frac{c}{c_h} \right) \exp \left(\frac{\eta}{b} \right) \quad [3]$$

Here t is time, x is the distance through the cell with $x = 0$ located at the membrane/CCL interface, η is the local (positive by convention) overpotential of the oxygen reduction reaction (ORR), j is the local proton current density in the CCL, C_{dl} is the double layer capacitance, i_* is the volumetric exchange current density of the electrode (A cm^{-3}), c is the local oxygen concentration, c_h is the oxygen concentration in the channel, b is the ORR Tafel slope, σ_p is the CCL proton conductivity and D is the oxygen diffusion coefficient in the CCL. The GDL model is simply a linear mass balance equation for

the oxygen concentration c_b in the GDL:

$$\frac{\partial c_b}{\partial t} - D_b \frac{\partial^2 c_b}{\partial x^2} = 0 \quad [4]$$

where D_b is the oxygen diffusion coefficient in the GDL. Note that Eqs. 3, 4 imply Fick's law for the oxygen flux. At the CCL/GDL interface, we request continuity of the oxygen concentration and flux; at the membrane interface we fix zero oxygen flux and the total ORR overpotential, at the CCL/GDL interface we request zero proton current and in the channel we fix the oxygen concentration.

Assuming small amplitude of the applied perturbation, the model (1)–(4) has been linearized and Fourier–transformed. The resulting system of linear equations for the perturbation amplitudes has been solved analytically, assuming that the steady–state shapes of the ORR overpotential and oxygen concentration are constant along the coordinate x. This assumption limits the cell current density, for which the model is applicable; the exact criterium is given below.

While the static shapes are assumed to be independent of x, the perturbation amplitudes are treated as the x–dependent variables. Physically, this combination means that the model is designed to capture *small* contributions of the proton and oxygen transport to the total CCL impedance. If the cell current is sufficiently small, the main contribution to the cell impedance gives the Tafel (charge–transfer) impedance. The corrections due to the transport processes are small, but finite and an accurate least–squares algorithm is able to capture these corrections.[4]

The analytical solution to equations for the perturbation amplitudes was used to calculate the total impedance of the cathode side Z_{tot}. The exact expression for Z_{tot} is rather bulky,[4] but it does not contain special functions and hence it is sufficiently "fast" for using in a least–squares algorithm. Calculation of zero–frequency limit of the impedance Z_{tot} leads to the total static differential resistivity R_{tot} of the cathode side:[4]

$$R_{tot} = \frac{l_t}{3\sigma_p} + \frac{b}{j_\phi} + \frac{bl_t}{3(4FDc_h)} + \frac{bl_b}{4FD_bc_h}, \quad j_\phi \ll \frac{\sigma_p b}{l_t} \quad [5]$$

Eq. 5 has been obtained by calculating $\lim_{\Omega \to 0} Z_{tot}$, where Z_{tot} is given by the dimensional version of Eq. [26] in[4] and Ω is the reduced dimensionless frequency of the exciting signal (Eq. [24] in[4]). The resulting expression has been expanded in Taylor series over the dimensionless cell current density, which at leading order gives Eq. 5.

Here l_t is the CCL thickness, j_ϕ is the cell current density and l_b is the GDL thickness. The first and second terms on the right side of Eq. 5 are the CCL proton resistivity and the Tafel resistivity, respectively. The third and fourth terms are the resistivities due to the oxygen transport in the CCL and the GDL, respectively. The term "Tafel resistivity" is introduced, as b/j_ϕ in Eq. 5 can be obtained by differentiation of the Tafel equation for the ORR activation overpotential

$$\eta_a = b \ln \left(\frac{j_\phi}{i_* l_t} \right) \quad [6]$$

over j_ϕ.

The model discussed is valid provided that the cell current density j_ϕ obeys to the condition

$$j_\phi \ll \min \left\{ j_* = \frac{\sigma_p b}{l_t}, j_D = \frac{4FDc_h}{l_b} \right\} \quad [7]$$

The current densities j_* and j_D characterize the rates of the proton and oxygen transport, respectively, through the CCL. If the cell current is much less than the minimal of the two, the contributions of both the transport processes to the cell impedance are small. Note that our goal is to capture these small contributions in order to find the respective transport coefficients σ_p and D, and hence an optimal for measurements current density is close to the upper limit prescribed by Eq. 7.

All the transport terms in Eq. 5 are independent of the cell current density j_ϕ. Thus, simply multiplying these terms by j_ϕ, we get the

respective transport overpotentials:

$$\eta_p = \frac{l_t j_\phi}{3\sigma_p}, \quad \text{proton transport} \qquad [8]$$

$$\eta_D = \frac{b l_t j_\phi}{3(4FDc_h)}, \quad \text{oxygen transport in the CCL} \qquad [9]$$

$$\eta_b = \frac{b l_b j_\phi}{4FD_b c_h}, \quad \text{oxygen transport in the GDL} \qquad [10]$$

The Tafel resistivity b/j_ϕ in Eq. 5 represents the contribution of the Tafel slope to the cell differential resistivity. This term does not take into account a constant shift of the cell polarization curve along the potential axis due to the exchange current density. At finite cell currents, this shift does not change the slope of the curve and hence it cannot be captured by impedance measurements discussed above. In other words, Eq. 5 per se does not allow us to calculate the ORR activation overpotential η_a. However, from the static analysis it follows, that at small j_ϕ, this overpotential is given by the Tafel equation (6). Clearly, Eq. 6 can be obtained by formal integration of the Tafel term in Eq. 5 with the lower limit of integration $i_* l_t$:

$$\eta_a = \int_{i_* l_t}^{j_\phi} \frac{b}{j_\phi} dj_\phi \qquad [11]$$

The volumetric ORR exchange current density i_* can be measured by EIS when the cell operates close to the open–circuit potential (see Ref. 53 for further discussion). Alternatively, i_* can be estimated by fitting the model[54] to the static polarization curve.

Fitting procedure.— Fitting has been performed in Maple environment using the built–it procedure *NonlinearFit*. The code reported in[4] has been modified as following. Figure 2 shows the raw impedance spectra for the segments 1–3 (the points with the positive imaginary part are not shown, see below). As can be seen, the spectra contain two arcs: a large low–frequency (LF) arc and a small arc in the high–frequency (HF) domain. We attribute the LF arc to the basic faradaic and transport processes in the system. The HF arc has been reported in many experiments; yet, however, the origin of this arc has not been clearly understood.[55,56] Our test measurement of impedance of the cell fed with hydrogen on both sides (H_2/H_2 feed) has shown that this arc disappears. This suggests that the HF arc in Figure 2 is caused by the processes on the cathode side in the presence of oxygen.

The HF arc of unknown origin has been taken into account by adding a simple parallel RC–circuit to the model impedance[4] for the "CCL+GDL" system (Figure 3). The parameters R and C can easily be found using the trial–and–error method. Once determined, the same R and C pair has been fixed for all the segments (Table I).
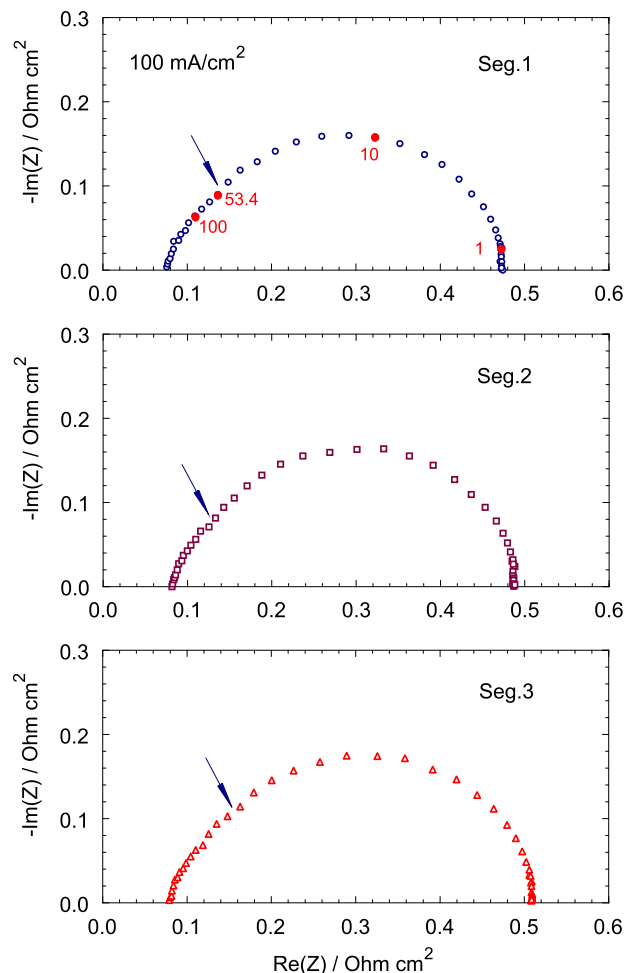

Figure 2. The raw impedance spectra for the segments 1–3. Arrows indicate the connecting point of the HF and LF arcs. Filled circles and numbers in the top frame indicate the characteristic points and the corresponding frequencies (f, Hz).
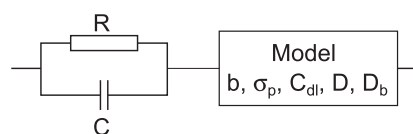

Figure 3. Transmission line with the parallel RC–circuit and the physical model for the "CCL+GDL"[4] connected in series.

Table I. Physical parameters of the cell resulted from impedance spectra fitting. The second column ("raw spectra") shows the results of fitting of the "raw" H_2/O_2 spectra. The last column corresponds to the spectra, which have been corrected by subtracting the respective H_2/H_2 spectra. The rows "RC–circuit..." indicate the parameters of the RC–circuit in Figure 3. To obtain the Tafel slope in units mV/decade, the values in this Table should be multiplied by 2.3.

	raw spectra	H_2/H_2–corrected spectra
Tafel slope b, mV	34.0	33.8
Apparent CCL proton conductivity σ_p, Ω^{-1} cm^{-1}	0.0534	0.0430
Double layer capacitance C_{dl}, F cm^{-3}	25.5	26.0
CCL oxygen diffusivity D, cm^{-3} s^{-1}	$0.454 \cdot 10^{-4}$	$0.457 \cdot 10^{-4}$
Proton transport loss η_p, mV	0.93	
Oxygen transport loss in the CCL, η_D, mV	2.3	
Characteristic current density j_*, A cm^{-2}	1.2	
Characteristic current density j_D, A cm^{-2}	0.5	
RC–circuit capacitance C, F cm^{-3}		$1.55 \cdot 10^{-3}$
RC–circuit resistance R, Ω cm^{2}		$4.13 \cdot 10^{-2}$
Oxygen molar concentration in the channel, mol cm^{-3}		$4.25 \cdot 10^{-5}$

Results and Discussion

Fitting parameters.— Before fitting, the raw impedance spectra were pre–processed according to the following protocol. The part of the spectrum corresponding to the highest frequencies is affected by the cable inductance; hence the HF points with the positive imaginary part of impedance have been ignored. Further, the experimental spectra were shifted to the left, so that in the leftmost point $\Re(Z) = 0$. This procedure removes the trivial constant shift of the spectra along the real axis due to ohmic resistances. Finally, the circuit in Figure 3 was fitted to the spectra.

Figure 4 shows the experimental and fitted curves for all the segments. The quality of fitting is good; a small gap between the points and the curves around the top of the LF semicircle is most probably

due to the small spatial variation of the static oxygen concentration and overpotential through the CCL depth, which is ignored in the model. At larger currents, this variation leads to strong depression of the faradaic arc.[54] Fitting of the HF part of the spectra is less accurate due to the effect of the cable inductance. The HF part is usually used to determine the CCL proton conductivity σ_p;[57] however, σ_p is also determined by the position of the main faradaic arc, and hence an accurate resolution of the HF straight line is not necessary (see discussion below).

The parameters resulted from fitting are gathered in Table I and shown graphically in Figure 5. The average over the cell surface values are indicated in Figure 5 by dotted lines.

The ORR Tafel slope exhibits variation between 31 and 37 mV (71 to 85 mV/decade), which most probably is caused by a small variation
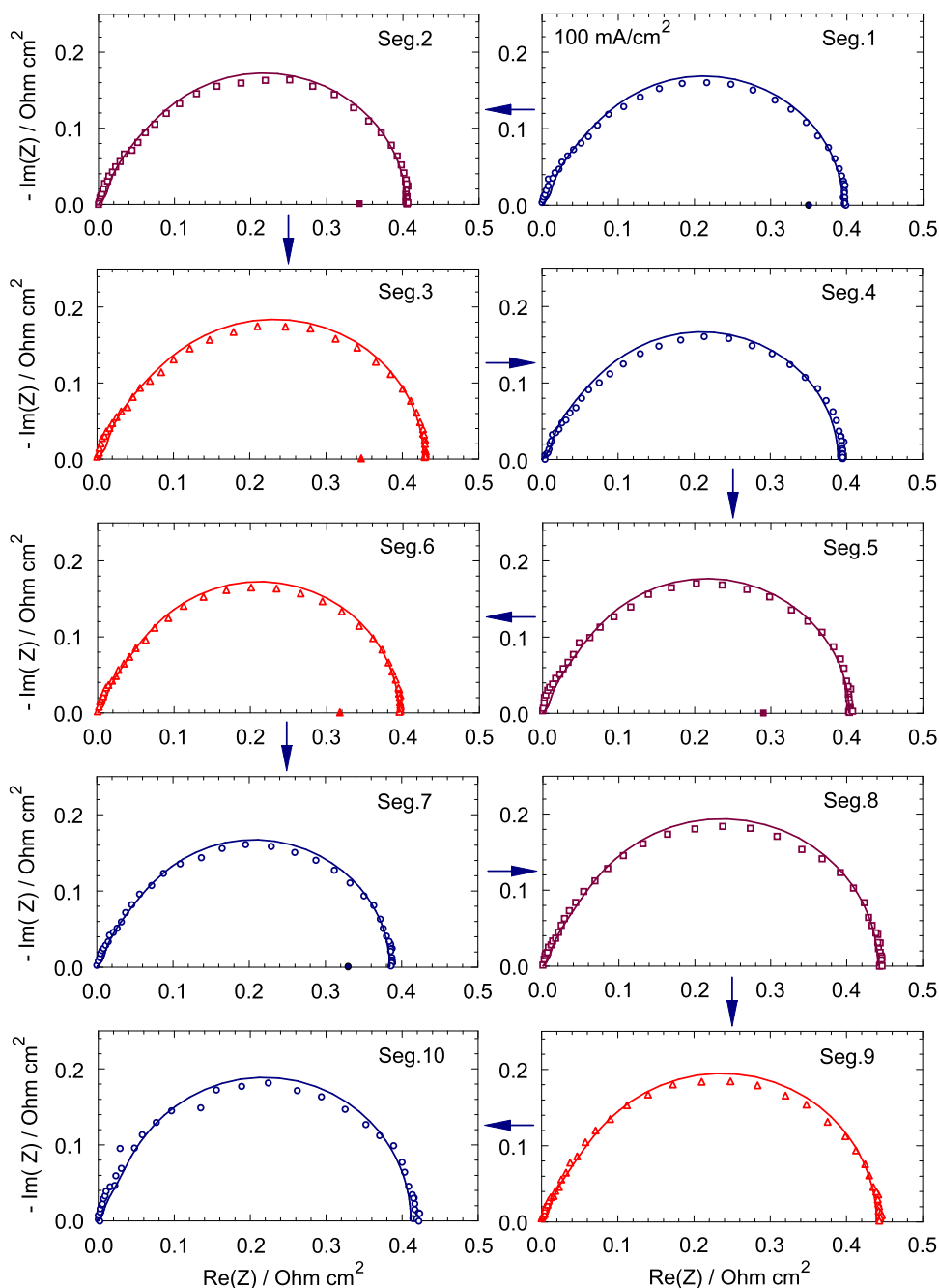

Figure 4. The experimental (points) and fitted (lines) spectra. Oxygen inlet is at segment 1; arrows indicate the direction of the oxygen flow. The IR–corrected DC resistivities of the segments 1–3 and 5–7 determined from the polarization curve fitting are indicated by filled symbols on the real axis.
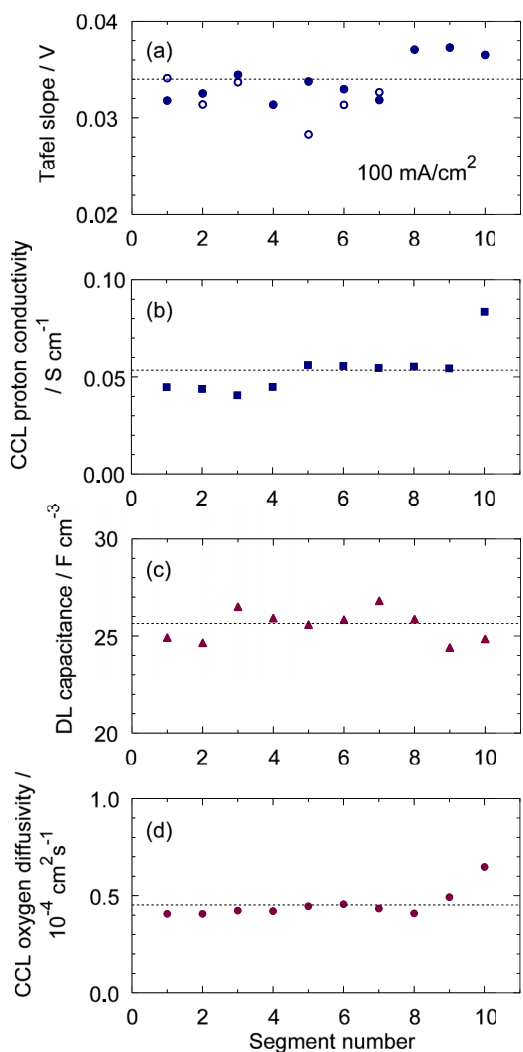
Figure 5. The fitting parameters for the segments 1–10. Open circles in (a) show the Tafel slopes determined from fitting the polarization curves (Figure 6); all the other points are obtained from fitting the impedance spectra.

The double layer capacitance C_{dl} varies between 24 and 27 F cm^{-3}, with the average of 25.5 F cm^{-3} (Figure 5c). This value is not far from $C_{dl} \simeq 15$ F cm^{-3} reported for similar systems.[57] Note that C_{dl} is a characteristic of electrochemically active surface of the electrode, which depends on many factors, like Pt loading, I/C ratio, water content etc.

The oxygen diffusion coefficient in the CCL is nearly constant along the cell surface, with the average over the segments value of $0.454 \cdot 10^{-4}$ cm^2 s^{-1} (Figure 5d). To the best of our knowledge, in low–temperature PEM fuel cells, this parameter has not been measured in situ so far. Note that D of $0.454 \cdot 10^{-4}$ cm^2 s^{-1} is ca. 30 times lower, than the value reported from ex situ measurements in a dry CCL.[62] This suggests strong effect of liquid water produced in the ORR, which fills the pores in the CCL. Indeed, measured D is nearly equal to the oxygen diffusion coefficient in liquid water,[63] which is $0.53 \cdot 10^{-4}$ cm^2 s^{-1} at 80°C. The transport overpotentials (8) and (9) calculated with the fitting parameters are listed in Table I. As can be seen, the MEA transport properties are well balanced, as η_p and η_D are close to each other (Table I).

Unfortunately, the model was unable to capture the oxygen diffusion coefficient in the GDL D_b. Under pure oxygen feed, the oxygen transport loss in the GDL is very small and the respective contribution to the cell impedance seemingly is below the accuracy of measurements. Note that the spectra of high–temperature PEMFC measured with air feed enabled to determine D_b using the same model.[4]

Verification of results.— To check the consistency of the fitting results, it is important to calculate the resulting characteristic current densities for the proton j_* and oxygen j_D transport in the CCL, Eq. 7. With the data from Table I, we get $j_* = 1.2$ A cm^{-2} and $j_D = 0.5$ A cm^{-2}. As the spectra have been collected at $j_\phi = 0.1$ A cm^{-2}, the relation (7) holds and hence the model is applicable.

To verify the results, separate impedance measurements of the cell fed with hydrogen on both sides have been performed. The pressure and humidity conditions were identical with those used in H$_2$/O$_2$ experiments. The H$_2$/H$_2$ spectrum for each segment has been subtracted from the respective spectrum for the H$_2$/O$_2$ feed. This correction minimizes the effect of cables on the impedance. The corrected spectra have been fitted using the same circuit in Figure 3. The resulting fitting parameters are listed in the last column in Table I. Due to reduced cable contribution in the HF domain, the apparent CCL proton conductivity is 20% less, than in the non–corrected spectra; the other parameters practically do not change (Table I).

Next, we calculated the total differential resistivity of the cathode side from the static polarization curves. The model[64] has been fitted to IR–corrected experimental curves of individual segments. This model is essentially an approximate analytical solution for the steady–state version of the system (1)–(4) valid for arbitrary cell currents. The results of polarization curve fitting for the segments 1–3 are shown in Figure 6. Successful fitting has been obtained for the segments 1–3 and 5–7, while in segments 4 and 8–10, the uncertainty due to poor accuracy of measured cell currents close to the open–circuit potential was too high. The Tafel slopes in the individual segments determined from the polarization curve fitting are depicted in Figure 5a by open circles. On average, the "static" Tafel slope data in Figure 5a are in good agreement with the data obtained from the impedance spectra.

Further, the fitted polarization curves have been differentiated over j_ϕ and the DC resistivity of the segments corresponding to the mean current density of 0.1 A cm^{-2} has been calculated. The respective points are indicated by filled symbols on the real axes in Figure 4. As can be seen, these values are about 15% lower, than the rightmost points of the impedance spectra, where $\Im(Z) = 0$. Makharia et al. suggested that the DC resistivity of the CCL given by the slope of the polarization curve differs from the rightmost point of the impedance spectrum due to inductance–like slow dynamics of adsorbates on a Pt surface.[57] In our experimental conditions, this 15%–discrepancy could rather be attributed to the systematic error due to differentiation of the fitted polarization curves. In the region of small cell currents,

of the local current between the segments (Figure 5 a). The segmented cell system is operated under control of the total cell current, while local currents may deviate from the mean value due to non–uniform distribution of the clamping pressure and inhomogeneities in electrochemically active surface area of the MEA. The average $b = 34$ mV (Table I) agrees with $b = RT/(\alpha F) = 30$ mV, with the transfer coefficient $\alpha = 1$ reported for the similar system.[58] Note that here we use the Tafel slope b per exponential basis; to obtain the value in units of mV/decade, the numbers in Table I should be multiplied by 2.3.

The CCL proton conductivity σ_p is nearly the same in all the segments, except segment 10 (Figure 5b). However, the impedance data for this segment are less accurate (Figure 4), which explains the jump in σ_p. A feature of this MEA is a high $\sigma_p \simeq 0.054$ Ω^{-1} cm^{-1}, which is almost an order of magnitude larger, than the values reported in.[57,59] Generally, σ_p is a strong function of the ionomer/carbon (I/C) ratio and of the electrode relative humidity.[60] For example, in a system with I/C=1/1, the conductivity σ_p varies in the range of 10^{-4} Ω^{-1} cm^{-1} to 0.03 Ω^{-1} cm^{-1}, depending upon the electrode water content.[60]

High value of σ_p in our MEA can be explained by a large amount of liquid water in the CCL. This is consistent with the low value of the oxygen diffusion coefficient in the CCL (see below). It is worth noting that collective mechanisms of proton conduction in a thin Nafion film covering Pt/C agglomerates could also increase σ_p.[61]
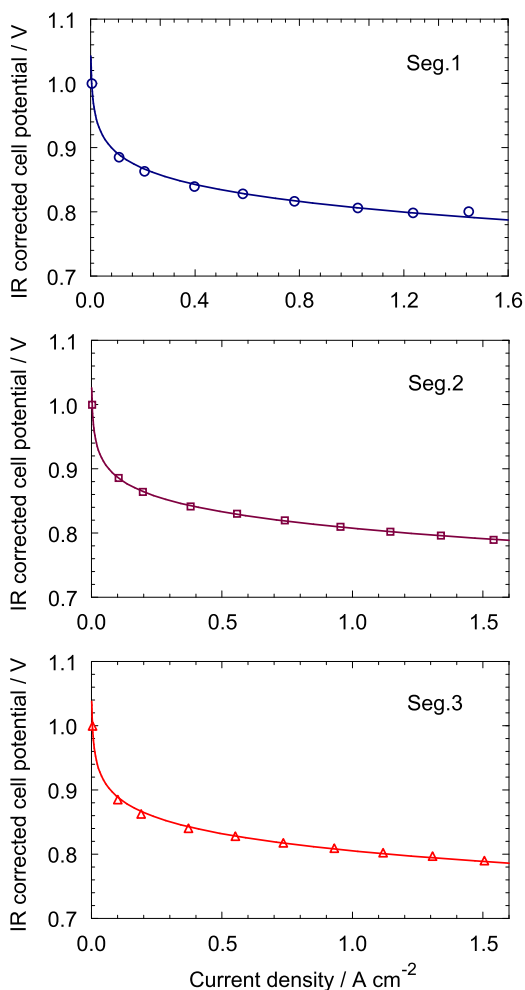
Figure 6. Measured (points) and fitted (lines) polarization curves of the segments 1–3. The Tafel slopes resulted from polarization curves fitting are indicated in Figure 5 a by open circles.

the IV–curve rapidly decays, and calculation of the curve slope is not quite reliable.

Remarks.— Makharia et al. emphasized the necessity to minimize the artificial (cable) inductance in order to get a clear straight 45°–line in the HF domain.[57] They used projection of this line onto the real axis to determine the CCL proton conductivity. However, though good resolution of this straight line is desirable, it is not necessary. The *length* of this straight line depends on σ_p: the lower σ_p, the larger the length. Thus, the straight 45°–line shifts the spectrum as a whole along the real axis, and hence the position of the faradaic arc contains information on the conductivity σ_p. Recently, it has been shown, that fitting of the low–frequency *half* of the impedance spectrum, from the top of the faradaic semicircle to the zero–frequency point, gives the proton conductivity of the CCL.[65]

The CCL oxygen diffusivity above is an effective parameter, which incorporates all the mechanisms of oxygen transport in the CCL. Breaking this parameter into contributions due to O_2 transport in voids, in Nafion film covering the Pt/C agglomerates, and in water filling the agglomerates would require a much more detailed structural model of the CCL. However, the effective parameter D may serve as an indicator of the CCL transport properties. In particular, measuring D before and after an accelerated stress testing may give useful hints on what has happened to the global structure of the CCL during the test.[66]

Conclusions

The model[4] has been fitted to impedance spectra acquired in a single run of a segmented PEM fuel cell operated at a high stoichiometry of the oxygen flow. Fitting directly gives the basic transport and kinetic parameters of the cathode catalyst layer. In the studied MEA, these parameters are: the Tafel slope $b \simeq 34$ mV, the apparent CCL proton conductivity $\sigma_p \simeq 0.053$ Ω^{-1} cm^{-1}, the double layer capacitance $C_{dl} \simeq 25$ F cm^{-3} and the CCL oxygen diffusivity $D \simeq 0.45 \cdot 10^{-4}$ cm^2 s^{-1}.

List of Symbols

b	Tafel slope, V
C_{dl}	Double layer volumetric capacitance, F cm^{-3}
c	Oxygen molar concentration in the CCL, mol cm^{-3}
c_b	Oxygen molar concentration in the GDL, mol cm^{-3}
c_h	Oxygen molar concentration in the channel, mol cm^{-3}
D	Oxygen diffusion coefficient in the CCL, cm^2 s^{-1}
D_b	Oxygen diffusion coefficient in the GDL, cm^2 s^{-1}
F	Faraday constant
j	Local proton current density, A cm^{-2}
j_ϕ	Cell current density, A cm^{-2}
j_*	Characteristic current density for proton transport, A cm^{-2}
j_D	Characteristic current density for oxygen transport in the catalyst layer, A cm^{-2}, Eq. 7
i_*	Volumetric exchange current density, A cm^{-3}
l_b	Gas–diffusion layer thickness, cm
l_t	Catalyst layer thickness, cm
R_{tot}	Total "CCL+GDL" resistivity, Ω cm^2, Eq. 5
x	Coordinate through the cell, cm
Z	Impedance, Ω cm^2

Greek

η_a	ORR activation overpotential, V
η_p	Proton transport overpotential, V
η_D	Overpptential due to the oxygen transport in the CCL, V
η_b	Overpptential due to the oxygen transport in the GDL, V
σ_p	CCL ionic conductivity, Ω^{-1} cm^{-1}

Subscripts

b	GDL
D	Oxygen diffusion in the CCL
p	Proton
t	Catalyst layer
$*$	Characteristic value

References

1. M. E. Orazem and B. Tribollet, *Electrochemical Impedance Spectroscopy*, Wiley, New–York, 2008.
2. A. Lasia, *Electrochemical Impedance Spectroscopy and its Applications*, Springer, New York, 2014.
3. H. Gerischer, *Z. Physik. Chem.*, **198**, 286 (1951).
4. A. A. Kulikovsky, *J. Electrochem. Soc.*, **162**, F217 (2015).
5. T. E. Springer, T. A. Zawodzinski, M. S. Wilson, and S. Gottesfeld, *J. Electrochem. Soc.*, **143**, 587 (1996).
6. Y. Bultel, L. Genies, O. Antoine, P. Ozil, and R. Durand, *J. Electroanal. Chem.*, **527**, 143 (2002).

7. F. Jaouen and G. Lindbergh, *J. Electrochem. Soc.*, **150**, A1699 (2003).
8. Q. Guo and R. E. White, *J. Electrochem. Soc.* **151** E133 (2004).
9. Y. Bultel, K. Wiezell, F. Jaouen, P. Ozil, and G. Lindbergh, *Electrochimica Acta*, **51**, 474 (2005).
10. D. Gerteisen, A. Hakenjos, and J. O. Schumacher, *J. Power Sources*, **173**, 346 (2007).
11. A. A. Franco, P. Schott, C. Jallut, and B. Maschke, *Fuel Cells*, **7**, 99 (2007).
12. M. Cimenti, D. Bessarabov, M. Tam, and J. Stumper, *ECS Transactions*, **28**, 147 (2010).
13. I. A. Schneider, M. H. Bayer, and S. von Dahlen, *J. Electrochem. Soc.* **158**, B343 (2011).
14. J. Mainka et al., *Fuel Cells*, **12**, 848 (2012).
15. J. R. Vang, S. J. Andreasen, and S. K. Kaer, *J. Fuel Cell Sci. Techn.*, **9**, 021005 (2012).
16. R. de Levie, Electrochemical response of porous and rough electrodes, in *Advances in Electrochemistry and Electrochemical Engineering*, edited by P. Delahay, volume 6, pages 329–397, Interscience, New–York, 1967.
17. A. Lasia, *J. Electroanal. Chem.*, **397**, 27 (1995).
18. A. Lasia, *J. Electroanal. Chem.*, **428**, 155 (1997).
19. M. Eikerling and A. A. Kornyshev, *J. Electroanal. Chem.*, **475**, 107 (1999).
20. S. J. C. Cleghorn, C. R. Derouin, M. S. Wilson, and S. Gottesfeld, *J. Appl. Electrochem.*, **28**, 663 (1998).
21. J. Stumper, S. A. Campbell, D. P. Wilkinson, M. C. Johnson, and M. Davis, *Electrochimica Acta*, **43**, 3773 (1998).
22. M. Noponen, T. Mennola, M. Mikkola, T. Hottinen, and P. Lund, *J. Power Sources*, **106**, 304 (2002).
23. M. Mench, C. Y. Wang, and M. Ishikawa, *J. Electrochem. Soc.* **150**, A1052 (2003).
24. Y.-G. Yoon, W.-Y. Lee, T.-H. Yang, G.-G. Park, and C.-S. Kim, *J. Power Sources*, **118**, 193 (2003).
25. L. C. Pérez, L. Brandão, J. M. Sousa, and A. Mendes, *Renewable and Sustainable Energy Reviews*, **15**, 169 (2011).
26. F. N. Büchi, A. B. Geiger, and R. P. Neto, *J. Power Sources*, **145**, 62 (2005).
27. I. A. Schneider, S. A. Freunberger, D. Kramer, A. Wokaun, and G. G. Scherer, *J. Electrochem. Soc.* **154**, B383 (2007).
28. I. A. Schneider, D. Kramer, A. Wokaun, and G. G. Scherer, *J. Electrochem. Soc.* **154**, B770 (2007).
29. F.-B. Weng, B.-S. Jou, C.-W. Li, A. Su, and S.-H. Chan, *J. Power Sources*, **181**, 251 (2008).
30. D. G. Sanchez and P. L. Garcia-Ybarra, *Int. J. Hydrogen Energy*, **37**, 7279 (2012).
31. R. Lin, E. Gülzow, M. Schulze, and K. A. Friedrich, *J. Electrochem. Soc.* **158**, B11 (2011).
32. T. V. Reshetenko, G. Bender, K. Bethune, and R. Rocheleau, *Electrochimica Acta*, **76**, 16 (2012).
33. T. V. Reshetenko, G. Bender, K. Bethune, and R. Rocheleau, *Electrochimica Acta*, **80**, 368 (2012).
34. L. C. Pérez, J. Ihonen, J. M. Sousa, and A. Mendes, *Fuel Cells*, **13**, 203 (2013).
35. Z. Liu, Z. Mao, C. Wang, W. Zhuge, and Y. Zhang, *J. Power Sources*, **160**, 1111 (2006).
36. D. Liang, Q. Shen, M. Hou, Z. Shao, and B. Yi, *J. Power Sources*, **194**, 847 (2009).
37. A. Lamibrac et al., *J. Power Sources*, **196**, 9451 (2011).
38. M. Dou et al., *J. Power Sources*, **196**, 2759 (2011).
39. D. J. L. Brett, P. Aguiar, N. P. Brandon, and A. R. Kucernak, *Int. J. Hydrogen Energy*, **32**, 863 (2007).
40. T. Tingelöf, L. Hedström, N. Holmström, P. Alvfors, and G. Lindbergh, *Int. J. Hydrogen Energy*, **33**, 2064 (2008).
41. T. Murahashi, T. Mitsumoto, and E. Nishiyama, *ECS Transactions*, **25**, 869 (2009).
42. K. F. A. M. M. Boaventura and H. Sander, *Electrochimica Acta*, **56**, 9467 (2011).
43. T. V. Reshetenko and J. St-Pierre, *J. Electrochem. Soc.* **161**, F1089 (2014).
44. M. Schulze, E. Gülzow, S. Schönbauer, T. Knori, and R. Reissner, *J. Power Sources*, **173**, 19 (2007).
45. T. V. Reshetenko, G. Bender, K. Bethune, and R. Rocheleau, *Electrochimica Acta*, **56**, 8700 (2011).
46. T. V. Reshetenko, G. Bender, K. Bethune, and R. Rocheleau, *Electrochimica Acta*, **69**, 220 (2012).
47. D. J. L. Brett et al., *Electrochem. Solid State Lett.* **6**, A63 (2003).
48. G. Bender, M. S. Wilson, and T. A. Zawodzinski, *J. Power Sources*, **123**, 163 (2003).
49. I. A. Schneider, H. Kuhn, A. Wokaun, and G. G. Scherer, *J. Electrochem. Soc.* **152**, A2092 (2005).
50. A. Hakenjos and C. Hebling, *J. Power Sources*, **145**, 306 (2005).
51. C. Wieser, A. Helmbold, and E. Gulzow, *J. Appl. Electrochem.*, **30**, 803 (2000).
52. D. J. L. Brett et al., *Electrochem. Comm.*, **3**, 628 (2001).
53. A. A. Kulikovsky, *J. Electroanal. Chem.*, **669**, 28 (2012).
54. A. A. Kulikovsky, *J. Electrochem. Soc.* **161**, E3171 (2014).
55. M. Keddam, C. Rakotomavo, and H. Takenouti, *J. Power Sources*, **161**, 920 (2006).
56. D. Malevich, E. Halliop, B. A. Peppley, J. G. Pharoah, and K. Karan, *J. Electrochem. Soc.* **156**, B216 (2009).
57. R. Makharia, M. F. Mathias, and D. R. Baker, *J. Electrochem. Soc.* **152**, A970 (2005).
58. K. C. Neyerlin, W. Gu, J. Jorne, and H. Gasteiger, *J. Electrochem. Soc.* **153**, A1955 (2006).
59. H. Makharia et al.,[57] determined the CCL proton resistivity R_p as a projection of the straight $45°$ HF line in the impedance spectra onto the real axis. This resistivity is given by the first term on the right side of Eq. 5, which gives σ_p.
60. Y. Liu et al., *J. Electrochem. Soc.* **156**, B970 (2009).
61. A. Golovnev and M. Eikerling, *Phys. Rev. E*, **87**, 062908 (2013).
62. J. Shen et al., *J. Power Sources*, **96**, 674 (2011).
63. P. Han and D. M. Bartels, *J. Chem. Phys.*, **100**, 5597 (1996).
64. A. A. Kulikovsky, *J. Electrochem. Soc.* **161**, F263 (2014).
65. A. A. Kulikovsky, *J. Electroanal. Chem.*, **738**, 108 (2014).
66. A. A. Kulikovsky, *Electrocatalysis*, **5**, 221 (2014).